CHEMISTRY OF MATERIALS
Article

Chem. Mater. **2009,** *21,* 3773–3781 3773
DOI:10.1021/cm8035136

Gold Nanoparticle Superlattices: Novel Surface Enhanced Raman Scattering Active Substrates

E. S. Shibu,[†] K. Kimura,[‡] and T. Pradeep*,[†]

[†]*DST Unit on Nanoscience (DST UNS), Department of Chemistry and Sophisticated Analytical Instrument Facility, Indian Institute of Technology, Madras, Chennai 600 036, India, and* [‡]*Graduate School of Material Science, University of Hyogo, 3-2-1 Koto, Kamigori-cho, Ako-gun, Hyogo 678-1297, Japan*

Received December 31, 2008. Revised Manuscript Received July 5, 2009

We developed a cheap and rapid method for the fabrication of 3D nanoparticle superlattices (SLs) of Au@SGAN and Au@MSA (*N*-acetyl glutathione (SGAN) and mercaptosuccinic acid (MSA) protected gold nanoparticles, respectively) in gram scale, at a liquid−liquid interfaces under flowing nitrogen gas. While available methods take several weeks to make crystalline SLs, the present route makes them in a day. Morphology of these crystals was examined with scanning electron microscopy (SEM), and their structures were probed using transmission electron microscopy (TEM). The surface enhanced Raman scattering (SERS) studies of these crystals were done using crystal violet (CV) molecules as the analyte which exhibited a detection limit of 10^{-8} M. The SERS spectrum was used to map the Raman images of the superlattce crystals. SERS from the edges of the crystal showed more enhancement than from the flat surfaces, which is in good agreement with theoretical reports of such anisotropic structures. The sides of the crystals are not sharp, and they show corrugations at the nanometer scale. This helps to produce more "hot spots" at the edges, which result in larger electric field enhancement from these locations. The enhancement factors (EF) for Au@MSA and Au@SGAN SLs were calculated to be around 1.47×10^6 and 3.60×10^5, respectively. More enhancements from Au@MSA SL compared to that of Au@SGAN could be attributed to the smaller chain length of the MSA molecule, which allows closer analyte approach to the nanoparticle surface.

Introduction

Surface enhanced Raman scattering (SERS) promises extraordinary potential for the detection of a range of molecules such as pesticides[1] and explosives[2] as well as biological objects such as DNA[3,4] and anthrax spores.[5] It is widely used in areas such as enzyme immunoassay,[6] detection of protease activity,[7] etc. Single molecule surface enhanced Raman scattering (SMSERS) was first observed by Nie, Emory, and Kneipp.[8,9] For the detection of a single molecule, a very high enhancement factor of about $10^{14}-10^{15}$ is required.[10−16] One of the promising approaches for the design of SERS substrates is the fabrication of nearly adjacent metallic nanostructures with a nanoscale gap. A possible system to build such structures is self-assembled monolayers of gold and silver nanoparticles. SERS from a 1D assembly of silver nanoparticles was studied.[17] Fabrication of periodic self-assembled three-dimensional (3D) superlattices (SLs) and the investigation of their collective properties have been fascinating developments in the science of nanomaterials.[18−22] SL formation of metal or semiconductor nanoparticles is being achieved by a simple bottom-up assembly, which includes the electrostatic self-assembly

*Corresponding author. Fax: + 91-44 2257-0545. E-mail: pradeep@iitm.ac.in.

(1) Weibenbacher, N.; Lendl, B.; Frank, J.; Wanzenböck, H. D.; Mizaikoff, B.; Kellner, R. *J. Mol. Struct.* **1997**, *410−411*, 539.
(2) Docherty, F. T.; Monagham, P. B.; McHugh, C. J.; Gramam, D.; Smith, W. E.; Cooper, J. M. *IEEE Sens. J.* **2005**, *5*, 632.
(3) Kneipp, K.; Kneipp, H.; Kartha, V. B.; Manoharan, R.; Deinum, G.; Itzkan, I.; Dasari, R. R.; Feld, M. S. *Phys. Rev. E* **1998**, *57*, 6281.
(4) Faulds, K.; Smith, W. E; Graham, D. *Anal. Chem.* **2004**, *76*, 412.
(5) Zhang, X.; et al. *J. Am. Chem. Soc.* **2005**, *127*, 4484.
(6) Dou, X.; Takama, T.; Yamaguchi, Y.; Ozaki, H. Y. *Anal. Chem.* **1997**, *69*, 1492.
(7) Ingram, A.; Byers, L.; Faulds, K.; Moore, B. D.; Graham, D. *J. Am. Chem. Soc.* **2008**, *130*, 11846.
(8) Nie, S.; Emory, S. R. *Science* **1997**, *275*, 1102.
(9) Kneipp, K.; Wang, Y.; Kneipp, H.; Perelman, L. T.; Itzkan, I.; Dasari, R. R.; Feld, M. S. *Phys. Rev. Lett.* **1997**, *78*, 1667.
(10) Krug, J. T.; Wang, G. D.; Emory, S. R.; Nie, S. *J. Am. Chem. Soc.* **1999**, *121*, 9208.
(11) Kneipp, K.; Kneipp, H.; Itzkan, I.; Dasari, R. R.; Feld, M. S. *Chem. Rev.* **1999**, *99*, 2957.
(12) Xu, H.; Aizpurua, J.; Käll, M.; Apell, P. *Phys. Rev.* **2000**, *E62*, 4317.
(13) Michaels, M.; Nirmal, M.; Brus, L. E. *J. Am. Chem. Soc.* **1999**, *121*, 9932.
(14) Michaels, M.; Nirmal, M.; Brus, L. E. *J. Phys. Chem. B* **2000**, *104*, 11965.
(15) Futamata, M.; Maruyama, Y.; Ishikawa, M. *Vib. Spectrosc.* **2002**, *30*, 17.
(16) Maruyama, Y.; Ishikawa, M.; Futamata, M. *Chem. Lett.* **2001**, 834.
(17) Luo, W.; Van der Veer, W.; Chu, P.; Mills, D. L.; Penner, R. M.; Hemminger, J. C. *J. Phys. Chem. C* **2008**, *112*, 11609.
(18) Collier, C. P.; Vossmeyer, T.; Heath, J. R. *Annu. Rev. Phys. Chem.* **1998**, *49*, 371.
(19) Gur, I.; Fromer, N. A.; Geier, M. L.; Alivisatos, A. P. *Science* **2005**, *310*, 462.
(20) Murray, C. B.; Kagan, C. R.; Bawendi, M. G. *Science* **1995**, *270*, 1335.
(21) Murray, C. B.; Kagan, C. R.; Bawendi, M. G. *Annu. Rev. Mater. Sci.* **2000**, *30*, 545.
(22) Shevchenko, E. V.; Talapin, D. V.; Kotov, N. A.; O'Brien, S.; Murray, C. B. *Nature* **2006**, *439*, 55.

Published on Web 07/31/2009

of oppositely charged nanoparticles of narrow size distribution,[23] evaporation of the solvent on a substrate,[24−35] self-organization of nanoparticles at interfaces,[36−39] crystallization of nanoparticles from nanoparticle dispersions by precipitation or sedimentation,[40,41] wet deposition by supramolecular interactions between the nanoparticles and a surface,[42−44] and self-assembly of nanoparticles into microdimensions through hydrogen bonding.[45−49] Among these methods, self-assembly through hydrogen bonding has achieved more attention since it provides uniform 3D SL crystals at the interface.[45−49]

Recently, we synthesized fluorescent molecule-tagged gold nanoparticle 3D SLs at air−water interface with a fluorescent dye, SAMSA (5-((2-(and-3)-*S*-(acetylmercapto)succinoyl)-amino)-fluorescein) covered nanoparticles.[50] But, the studies were limited due to the cost and unavailability of SAMSA. To overcome this problem, we synthesized dansyl glutathione (DGSH) from easily available dansyl chloride.[51] We performed numerous spectroscopic and microscopic studies on the Au@SGAN−SGD (*N*-acetyl glutathione (SGAN)) SL system and utilized the fluorescence of SLs for the selective detection of Bovine Serum Albumin (BSA) in nanomolar concentrations.[52]

These crystals could be new materials for SERS studies. This is because, in such an SL, nanometer scale voids exist in a periodic fashion due to the periodic arrangement of nanoparticles. In these locations, the electric field due to the surface plasmon resonance of the nanoparticles is expected to be large. It presents a new possibility for creating SERS active substrates through self-assembly. There have been attempts to obtain SERS from organized assemblies of gold and silver nanopartilces.[53,54] But, one of the drawbacks of this method is the time required for crystal formation; it is on the order of 2 months for the formation of high quality crystals at the air−water interface.[45−49] But to bring these 3D nanostructures into application levels, materials should be available in gram scale and the method should be cheap. In this context, we developed a new method for the large scale synthesis of 3D SL of gold nanoparticles in a short time period. Although this approach is rapid for nanoparticles of this kind, there have been other approaches in which nanoparticle SL crystals have been made in a period of hours by hydrothermal and solvothermal methods.[55,56]

In this article, we present a simple and rapid method for the fabrication of 3D SLs at a liquid−liquid interface under flowing nitrogen gas. This method can be used to fabricate the 3D SLs in gram quantities in a short time scale. We also studied the SERS of these crystals using crystal violet (CV) as an analyte. We were able to detect CV up to a concentration of 10^{-8} M. The SERS spectrum collected from CV molecules adsorbed on the surface of the crystals was used to map the Raman image of the SL triangular crystals. The Raman image shows more enhancement at the edge of the triangular crystal compared to that at the surface, which is in good agreement with the theoretical reports.[57,58] The microscopic images of the SL crystals shows corrugations at the edges. This is due to the fact that crystals are formed by the layer-by-layer assembly of nanoparticles in a periodic fashion. This will make the edges of the triangles rougher, or in other words, it will create more hot spots accessible at the edges. This will make the SL triangles an interesting group of new materials, which can act as good platform for SERS studies with reasonably good enhancement. We note that an account of the efforts to synthesize quantum dots and nanoparticle films at liquid−liquid interfaces,[37,38,59] a field pioneered by Rao, has been presented recently.[60]

(23) Alexander, M.; Kalsin.; Fialkowski, M.; Paszewski, M.; Smoukov, S. K.; Bishop, K. J. M.; Grzybowski, B. A. *Science* **2006**, *312*, 420.
(24) Harfenist, S. A.; Wang, Z. L.; Whetten, R. L.; Vezmar, I.; Alvarez, M. M. *Adv. Mater.* **1997**, *9*, 817.
(25) Ohara, P. C.; Heath, J. R.; Gelbart, W. M. *Angew. Chem., Int. Ed. Engl.* **1997**, *36*, 1078.
(26) Shevchenko, E. V.; Talapin, D. V.; Kotov, N. A.; O'Brien, S.; Murray, C. B. *Nature* **2006**, *439*, 55.
(27) Taleb, A.; Petit, C.; Pileni, M. P. *Chem. Mater.* **1997**, *9*, 950.
(28) Daniel, M.-C.; Astruc, D. *Chem. Rev.* **2004**, *104*, 293.
(29) Rogach, A. L.; Talapin, D. V.; Shevchenko, E. V.; Kornowski, A.; Haase, M.; Weller, H. *Adv. Funct. Mater.* **2002**, *12*, 653.
(30) Redl, F. X.; Cho, K. S.; Murray, C. B.; O'Brien, S. *Nature* **2003**, *423*, 968.
(31) Stoeva, S. I.; Prasad, B. L. V.; Uma, S.; Stoimenov, P. K.; Zaikovski, V.; Sorensen, C. M.; Klabunde, K. J. *J. Phys. Chem. B* **2003**, *107*, 7441.
(32) Dabbousi, B. O.; Murray, C. B.; Rubner, M. F.; Bawendi, M. G. *Chem. Mater.* **1994**, *6*, 216.
(33) Stoeva, S.; Klabunde, K. J.; Sorensen, C. M.; Dragieva, I. *J. Am. Chem. Soc.* **2002**, *124*, 2305.
(34) Pileni, M. P. *J. Phys. Chem. B* **2001**, *105*, 3358.
(35) Weller, H. *Curr. Opin. Colloid Interface sci.* **1998**, *3*, 194.
(36) Binder, W. H. *Angew. Chem., Int. Ed.* **2005**, *44*, 5172.
(37) Sarathy, K. V.; Kulkarni, G. U.; Rao, C. N. R. *Chem. Commun.* **1997**, *6*, 537.
(38) Rao, C. N. R.; Kulkarni, G. U.; Thomas, P. J.; Agarwal, V. V.; Saravanan, P. *J. Phys. Chem B* **2003**, *107*, 7391.
(39) Lin, Y.; Skaff, H.; Emrick, T.; Dinsmore, A. D.; Russell, T. P. *Science* **2003**, *299*, 226.
(40) Alivisatos, A. P.; Johnson, K. P.; Peng, X.; Wilson, T. E.; Loweth, C. J.; Bruchez, M. P.; Schultz, P. G. *Nature* **1996**, *382*, 609.
(41) Talapin, D. V.; Shevchenko, E. V.; Kornowski, A.; Gaponik, N.; Haase, M.; Rogach, A. L.; Weller, H. *Adv. Mater.* **2001**, *13*, 1868.
(42) Boal, A. K.; Ilhan, F.; DeRouchey, J. E.; Thurn-Albrecht, T.; Russel, T. P.; Rotello, V. M. *Nature* **2000**, *404*, 746–748.
(43) Demer, L. M.; Ginger, D. S.; Park, S.-J.; Li, Z.; Chung, S.-W.; Mirkin, C. A. *Science* **2002**, *296*, 1836.
(44) Sanyal, A.; Norsten, T. B.; Uzun, O.; Rotello, V. M. *Langmuir* **2004**, *20*, 5958.
(45) Kimura, K.; Sato, S.; Yao, H. *Chem. Lett.* **2001**, *30*, 372.
(46) Wang, S. H.; Sato, S.; Kimura, k. *Chem. Mater.* **2003**, *15*, 2445.
(47) Wang, S. H.; Yao, H.; Sato, S.; Kimura, K. *J. Am. Chem. Soc.* **2004**, *126*, 7438.
(48) Yang, Y.; Liu, S.; Kimura, K. *Angew. Chem., Int. Ed.* **2006**, *45*, 5662.
(49) Yao, H.; Minami, T.; Hori, A.; Koma, M.; Kimura, K. *J. Phys. Chem B.* **2006**, *110*, 14040.
(50) Nishida, N.; Shibu, E. S.; Yao, H.; Oonishi, T.; Kimura, K.; Pradeep, T. *Adv. Mater.* **2008**, *20*, 4719.
(51) Gan, J.; Harper, T. W.; Hsueh, M.-M.; Qu, Q.; Humphreys, W. *Chem. Res. Toxicol.* **2005**, *18*, 896.
(52) Shibu, E. S.; Muhammed., M. A. H.; Kimura, K.; Pradeep, T. *Nano Res.* **2009**, *2*, 220–234.
(53) Wang, H.; Levin, C. S.; Halas, N. *J. Am. Chem. Soc.* **2005**, *127*, 14992.
(54) Gunnarsson, L.; Bjerneld, E. J.; Xu, H.; Petronis, S.; Kasemo, B.; Kall, M. *Appl. Phys. Lett.* **2001**, *78*, 802.
(55) Kim, Y. H.; Lee, D. K.; Cha, H. G.; Kim, C. W.; Kang, Y. S. *Chem. Mater.* **2007**, *19*, 5049.
(56) Gao, F.; Lu, Q.; Komarneni, S. *Chem. Mater.* **2005**, *17*, 856.
(57) Hao, E.; Schatz, G. C. *Chem. Phys.* **2004**, *120*, 357.
(58) Heynes, C. L.; McFarland, A. D.; Van Duyne, R. P. *Anal. Chem.* **2005**, *1*, 338A.
(59) Kalyanikutty, K. P.; Gautam, U. K.; Rao, C. N. R. *Solid State Sci.* **2006**, *8*, 296.
(60) Rao, C. N. R.; Kalyanikutty, K. P. *Acc. Chem. Res.* **2008**, *41*, 489.

Materials and Methods

Materials. All the chemicals were commercially available and used without further purification. $HAuCl_4 \cdot 3H_2O$, methanol (GR grade), ethanol (GR grade), and glutathione, (GSH, γ-Glu-Cys-Gly, MW = 307) were purchased from SRL Chemical Co. Ltd., India. $NaBH_4$ (>90%) and mercaptosuccinic acid (MSA, MW = 106) were purchased from Sigma Aldrich. Acylation of GSH leading to *N*-acetyl GSH (NAGSH) was performed using a reported procedure.[61] Deionized (DI) water with resistivity >18 MΩ cm was used for all the experiments.

Synthesis of Au@SGAN. The acronym Au@SGAN refers to Au nanoparticles protected with −SGAN groups. The procedure used here for the synthesis of Au@SGAN follows the reported protocol with a few modifications.[49] To a 200 mL methanolic solution of (5 mM) $HAuCl_4 \cdot 3H_2O$, 5 mM ligands were added. The mixture was cooled to 0 °C in an ice bath for 30 min. Then, an aqueous solution of $NaBH_4$ (0.2 M, 50 mL), cooled to 0 °C, was injected rapidly into the above mixture under vigorous stirring. The mixture was allowed to react for another hour. The resulting precipitate was collected and washed repeatedly with methanol through centrifugal precipitation. Finally, the Au@SGAN precipitate was dried and collected as a dark brown powder. This makes 8.5 nm mean diameter particles.

Synthesis of Au@MSA. Au@MSA nanoparticles were synthesized using a reported protocol with few modifications.[47,50] To make 8.5 nm mean diameter particles, we followed the following procedure. To a 50 mL methanolic solution of (5 mM) $HAuCl_4 \cdot 3H_2O$, 5 mM MSA was added (1:1 ratio, total volume of methanol was 200 mL). The mixture was cooled to 0 °C in an ice bath for 30 min. Then, an aqueous solution of $NaBH_4$ (0.2 M, 50 mL), cooled to 0 °C, was injected rapidly into the above mixture under vigorous stirring. The mixture was allowed to react for another hour. The resulting precipitate was collected and washed repeatedly with methanol through centrifugal precipitation. Finally the Au@MSA precipitate was dried and collected as a dark brown powder.[47,50] 3.5 nm particles can be made by using a different Au:S ratio.

Setup Used for the Fabrication of SL Crystals in Gram Scale. We developed a simple setup for the easy fabrication of SLs, which is shown in Scheme 1. It consisted of an airtight plastic box with an inlet and outlet. A nitrogen cylinder was connected to the inlet through a silicon tube. The gas exit was fitted with a paraffin oil filled trap.

Synthesis of Au@SGAN and Au@MSA SLs. Here, we used a modified method for the synthesis of Au@SGAN and Au@MSA SLs. The method is described below. We used two different sizes (3.5 and 8.5 nm) of Au@MSA and Au@SGAN nanoparticles (in each case) for the fabrication of SLs. For both the SLs, the procedure was the same. About 10 mg of Au@SGAN and Au@MSA nanoparticles were dissolved in 5 mL of water in separate beakers and the pH of the solutions was adjusted to 0.7−0.9 by adding 12 M HCl into the nanoparticle solution dropwise. To this acidic nanoparticle dispersion, 5 mL of toluene was added and solution was kept inside the setup described above under nitrogen atmosphere (stage 1). The paraffin oil-filled bubbler indicated a flow of two bubbles per second. The samples were left undisturbed for 2 days, in the dark at a temperature below 25 °C. The crystal formation started within a few hours at the toluene−water interface. Within 24 h, all the toluene evaporated and the SL films begin to form on top of the aqueous layer (stage 2). A thick film with mirrorlike appearance was seen within 48 h, indicating the formation of gold nanoparticle SLs with micrometer dimensions (stage 3). Different stages of the crystal formation have been photographed and are given along with the setup in Scheme 1. The top views of the grown SL film were also photographed and one picture is given in Scheme 1 (stage 3). The first step of the SL formation is the creation of an island having an ordered arrangement of nanoparticles. In the second step, other nanoparticles will get attached to the island to form a second layer. This will continue to yield morphologically different crystals. After the formation of SLs, SEM measurements were done by transferring the film onto polished silicon wafers. Raman measurements were done by transferring the film onto thin cover glass slips. Film samples were transferred on carbon coated copper grids and dried at room temperature for HRTEM measurements. A photograph of the setup is given in the Supporting Information (Figure S1).

Scheme 1. Schematic Representation of the Setup used for the SL Formation[a]

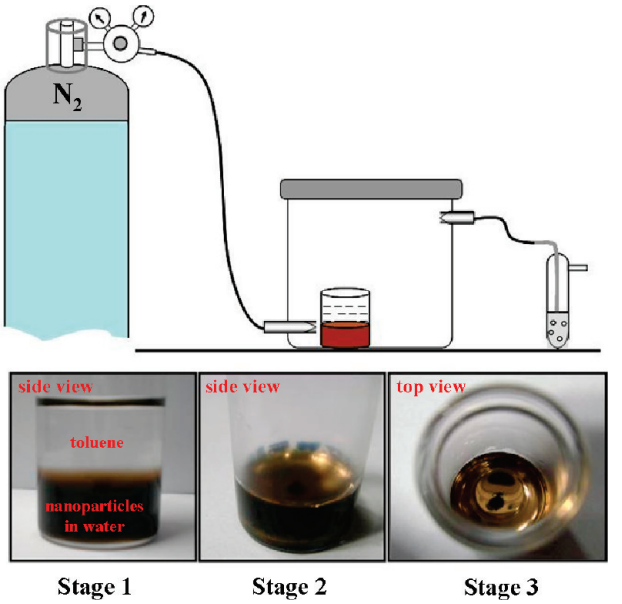

[a] The photographs show different stages of crystal formation. The top view of the SL crystals (stage 3) clearly shows a continuous film at the interface.

We also tried to construct the SLs under a flow of air instead of nitrogen gas. But, we did not observe any crystal formation at the same time scale, under the same flow rate. The reason for the formation of the crystals at the water−toluene interface with nitrogen gas flow is not known exactly. However, it appears that increased humidity retards crystal growth. Nanoparticles will form an island at the interface when the system is kept without disturbance. At the liquid−liquid interface, this occurs in a short period. The nanoparticles have a propensity to come to the interface as they are protected with surfactants. The rapid evaporation of the organic phase is likely to produce a reduced temperature at the interface which may also aid in crystallization around the islands. In the normal method, the process of the island formation occurs only within a period of 7−9 days. This has been checked in the same experimental setup in the absence of the toluene layer with nitrogen flow. At this condition, we could not see any crystal formation. But in the absence of nitrogen flow, we could see slow crystal formation after the evaporation of the toluene over layer. This is comparatively slow as in case of the old method. This clearly shows that gas

(61) Levy, E. J.; Anderson, M. E.; Meister, A. *Anal. Biochem.* **1993**, *214*, 135.

flow on the top of the nanoparticle dispersion will disturb the island formation. But we can avoid it by having an organic over layer. Instead of toluene, we tried other fast evaporating solvents such as hexane, diethyl ether, etc. The quality of the crystals formed using toluene as an interface was far better. Variation of the atmosphere above the liquid phase is known to affect SL formation.[48]

Methods. The Raman spectrum and corresponding imaging were done using a Witec GmbH confocal Raman spectrometer equipped with 514.5 and 532 nm sources with a spot size $< 1\ \mu$m. The laser had a maximum power of 40 mW. The excitation laser was focused using a 100× objective, and the signal was collected in a backscattering geometry and guided to a Peltier-cooled charge-coupled device (CCD) detector. The sample was mounted on a piezo-equipped scan stage to enable spectral imaging. Single-spot spectra were also acquired using the same grating but with larger integration times. For improved resolution and to ascertain the peak positions, a grating with 1800 grooves/mm was also used while acquiring single-spot spectra. The effective scan range of the spectrometer was 0−9000 cm^{-1} (amounts to a wavelength maximum of 958.2 nm for 514.5 nm excitation and 1020.70 nm for 532 nm excitation), with detection efficiency falling above 750 nm. For spectral imaging, the desired area was partitioned into 10 000 squares (an imaginary 100 × 100 matrix drawn over it), with each square representing a sampling point and consequently a pixel for the image. Typical signal acquisition time at each pixel of the image was 0.1 s. The intensities of the desired portion of the spectra, collected over all the pixels, were compared by Scan CTRL Spectroscopy Plus version 1.32 software to construct a color-code image. Spectral intensities acquired over a predefined area were automatically compared to generate color-coded images. In the images, regions coded yellow are with maximum intensities and regions shown in black are with minimum signal intensities. High-resolution transmission electron microscopy (HRTEM) images were collected using JEOL 3010 UHR instrument. The SL films were lifted on carbon coated copper grids and dried in ambience. The sample was observed at 200 keV to reduce electron beam induced damage. Scanning electron microscopy (SEM) and energy dispersive analysis of X-rays (EDAX) were carried out with a FEI QUANTA 200. We carefully lifted the SL film by using a copper wire loop and placed it on a polished silicon wafer or clean conducting glass. The samples were carefully washed with ethanol and left for drying for a few hours in the ambient air. The dried samples were mounted on the SEM stub, and conduction between the sample and the stub was facilitated with a conducting carbon tape. All the SEM measurements were done at 30 kV. Small angle X-ray spectroscopy (SAXS) measurements were performed with a Bruker-AXS NanoSTAR instrument. The instrument has an X-ray tube (Cu Kα radiation, operated at 45 kV/35 mA), cross-coupled Göbel mirrors, three-pinhole collimation, evacuated beam path, and a 2D gas-detector (HI-STAR).[62] Energy minimization of MSA and SGAN has been done using B3LYP functional[63] using the 6-31G* basis set.[64] For all of the studies, including HRTEM, SEM, SAXS and SERS, we used SLs of 8.5 nm diameter nanoparticles. Raman images presented in the text are from SLs of 3.5 nm diameter collected at 514.5 nm excitation, although SLs of 8.5 nm diameter were also used. Data were also collected with 532 nm excitation.

(62) Pedersen, J. S. *J. Appl. Crystallogr.* **2004**, *37*, 369.
(63) Becke, A. D. *J. Chem. Phys.* **1993**, *98*, 5648.
(64) Francl, M. M.; Pietro, W. J.; Hehre, W. J.; Binkley, J. S.; Gordon, M. S.; Defrees, D. J.; Pople, J. A. *J. Chem. Phys.* **1982**, *77*, 3654.

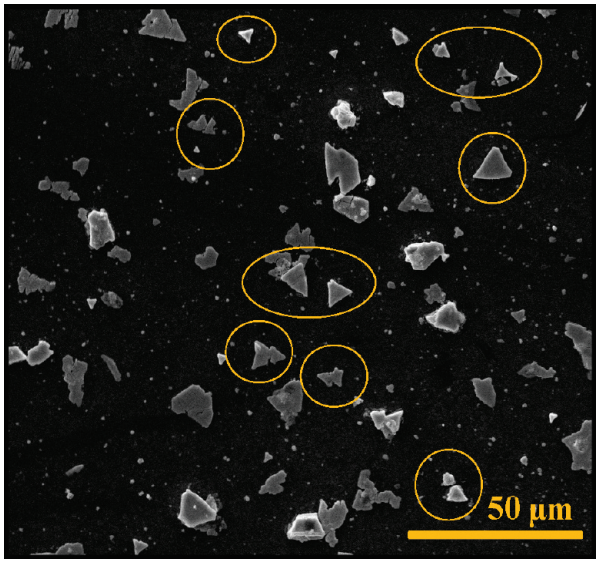

Figure 1. Large area SEM image of Au@SGAN SL triangles. The triangular morphologies are marked by circles and ellipses.

Results and Discussion

All the SL crystals were synthesized using gold nanoparticles with an average diameter of 8.5 nm. HRTEM images of Au@MSA and Au@SGAN nanoparticles are given in the Supporting Information (Figure S2). The particles are highly uniform. The morphology of the SLs was examined in great detail with SEM. Figure 1 shows one of the large area images of Au@SGAN SL crystals showing a large number of triangles (marked by circles and ellipses). In addition to triangles, we observed other morphologies also. In this large area image, we can see a few broken crystals too. Most of the crystals are triangular in morphology as reported earlier.[52] The typical edge length of these triangles is 6−8 μm. There are also irregular particles; long-range periodicity of particles was seen in them as well. Amorphous regions were rare. The large area SEM image of Au@MSA SLs was also examined, and it is given in the Supporting Information (Figure S3).

To understand the details of particle arrangements in the SL crystals, we analyzed the films by HRTEM. Figure 2A and B shows the TEM images of Au@SGAN and Au@MSA SLs, respectively. Due to the thickness of the crystal, we could analyze the particle arrangement only at the edges of the triangles, in contrast to our earlier papers where wider areas could be imaged.[50,52] In both cases, the particles show a truncated octahedral (TO) shape with {100} and {111} facets which are shown in the insets of the figures. In the images, a $[110]_{SL}$ projection of the unit cell of the SL is represented by a rectangular box, where the subscript SL refers to the SL. Figure 2 reveals that no further growth of nanoparticles occur in the SL crystal. The particle size is the same as that shown in Figure S2. The $[111]_{SL}$ spacing was found to be 12.3 and 10.4 nm in the SGAN and MSA SLs, respectively. The $[220]_{SL}$ spacing was found to be 7.5 and 6.4 nm in the SGAN and MSA SL crystals, respectively. All these values are in good agreement with the SAXS data.

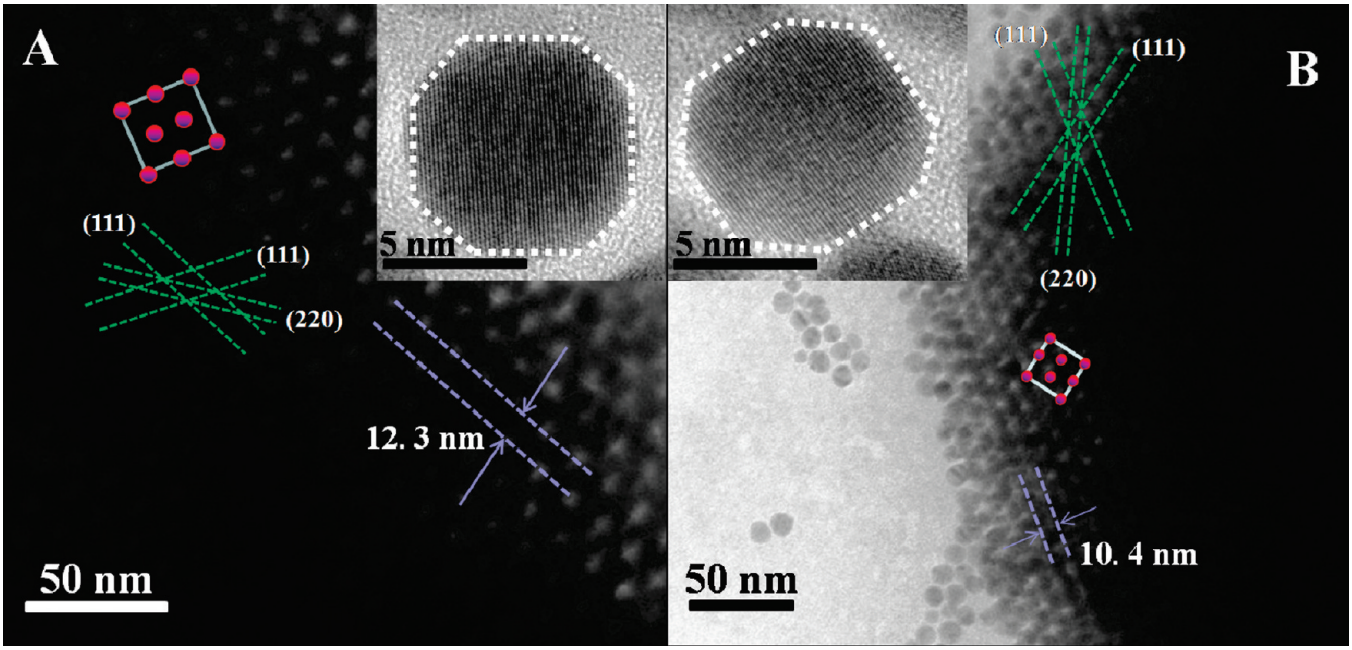

Figure 2. (A and B) HRTEM images of Au@ SGAN and Au@MSA SLs, respectively. The inset of each figure shows the truncated octahedral (TO) shape of the nanoparticles with {100} and {111} facets.

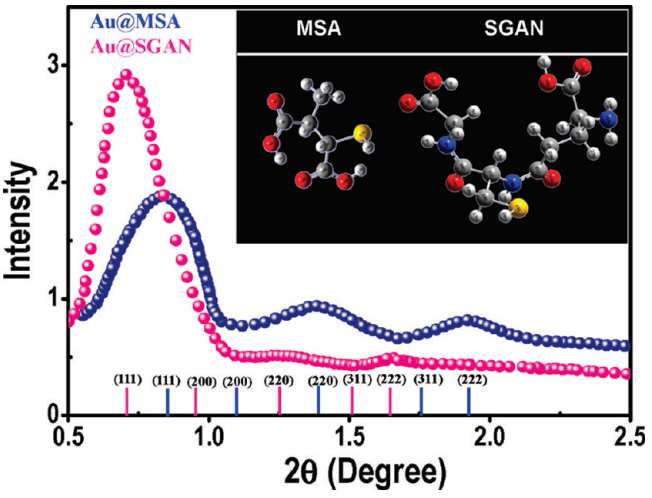

Figure 3. Background and baseline corrected intensity vs 2θ data of Au@SGAN and Au@MSA SLs, respectively. The indexing is done for a *fcc* unit cell in both cases. The inset shows the energy minimum structure of MSA and SGAN.

Superlattice images presented here are similar to the fringes shown in recent reports.[65,66]

Stacking of the nanoparticles in the 3D superlattices was characterized by SAXS. The superlattice samples were transferred to a thin mica sheet and dried in ambient conditions. As SAXS is a bulk measurement, different types of superlattice morphologies were investigated together. After the measurement, contribution of the mica background was subtracted. The data were measured overnight for each sample. Figure 3 shows intensity vs 2θ data obtained after background and baseline corrections (Au@SGAN and Au@MSA SLs). We see that the constituent gold nanoparticles are stacked in a *fcc* pattern rather than *hcp* in the 3D array in both cases. All the expected reflections are seen. In the case of Au@MSA, (111), (220), and (222) reflections appear as expected, and the (200) and (311) reflections are weak. For Au@SGAN, the crystals show preferential (111) orientation as expected from a majority of triangular morphologies shown in Figure 1 (note that the surfaces of all these crystals are (111)). Expected reflections and positions are indicated with sticks in Figure 3. While interplanar spacing for (111) and (220) of Au@MSA SL are 10.5 and 6.4 nm, respectively, for Au@SGAN SLs the values are 12.4 and 7.5 nm, respectively. All these parameters are in good agreement with HRTEM data as mentioned above.

Even though the particle size is the same in both nanoparticles, the interparticle (particle−particle) spacing is different (by 1.9 nm). This difference in the spacing is due to the difference in the dimensions of SGAN and MSA and also the variation in their molecular interactions. The effective molecular dimensions of SGAN and MSA are 1.8 and 0.7 nm, respectively (energy minimum structures calculated by density functional theory (DFT) are given in the inset of Figure 3). Variation in the length of the molecules itself contributes to a difference of 1.1 nm. Besides this, there is a possibility of different extent of water inclusion in these samples. Au@MSA SLs are known to contain water.[47] It is expected that there is greater anisotropy in the monolayer order in SGAN SLs in view of their greater molecular freedom.

In order to study the spatial distribution of gold in the SL film, elemental mapping of a single crystal was carried out using energy dispersive analysis of X-rays (EDAX).

(65) Zhuang, J.; Wu, H.; Yang, Y.; Cao, Y. C. *J. Am. Chem. Soc.* **2007**, *129*, 14166.
(66) Zhuang, J.; Wu, H.; Yang, Y.; Cao, Y. C. *Angew. Chem., Int. Ed.* **2008**, *47*, 2208.

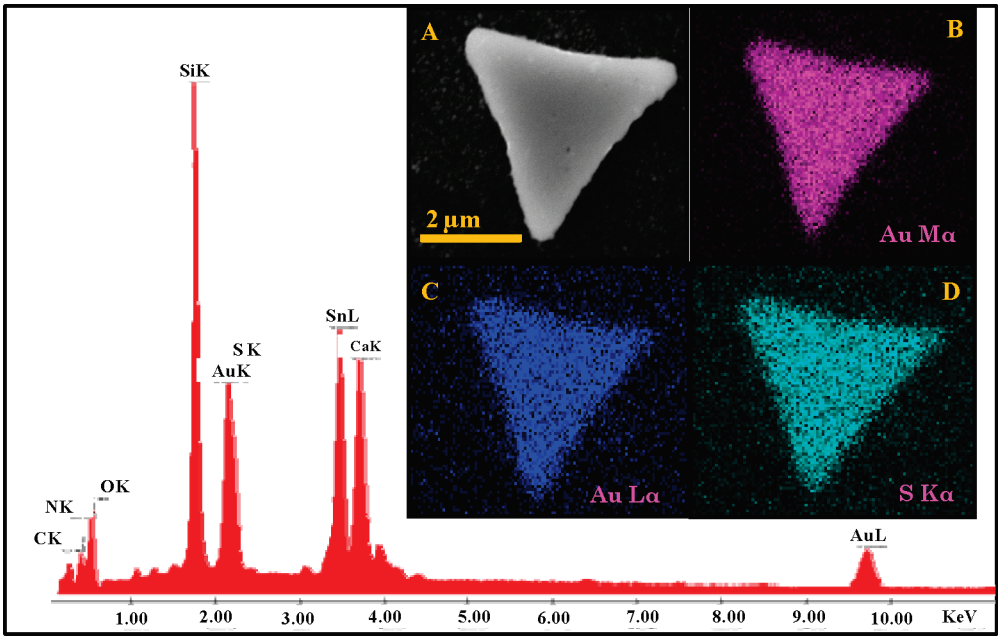

Figure 4. EDAX spectrum of Au@SGAN nanoparticle SL crystal shown in part A. (B−D) EDAX mapping of the triangle using Au Mα, Au Lα, and S Kα. The Si, Sn, and In peaks are due to the conducting glass substrate used.

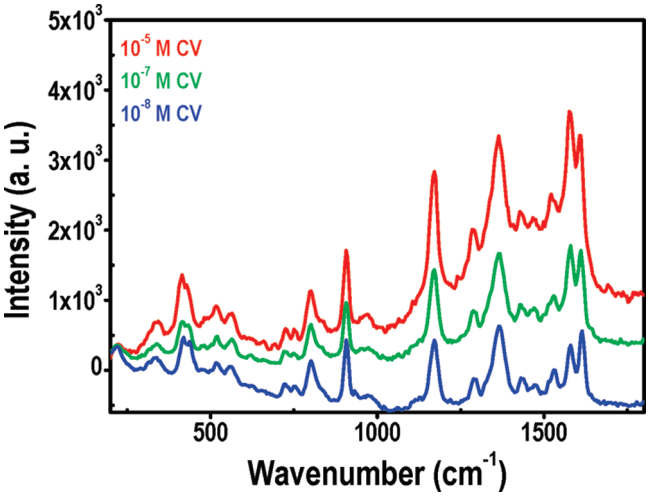

Figure 5. SERS spectra of CV collected from the surface of Au@MSA SL crystals excited using 532 nm, with an acquisition time of 4 s. The detection limit of CV was $\sim 10^{-8}$ M.

Figure 4 shows the EDAX spectrum collected from the SL triangle shown in Figure 4A. EDAX mapping was done using Au Mα, Au Lα, and S Kα and the images are given in Figure 4B−D. We also measured the SEM and elemental mapping of Au@MSA nanoparticle crystals and the data are given in the Supporting Information (Figure S4).

Surface Enhanced Resonance Raman Studies (SERS). The SERS studies were done using a Witec GmbH confocal Raman spectrometer. The SL crystals were transferred to a thin glass plate, washed with ethanol, and dried under ambient conditions. All the SERS measurements were done using crystal violet (CV) as the Raman marker molecule. The CV solutions were prepared in water at different concentrations (10^{-5}−10^{-8} M). The sample plates were dipped in CV solution of required concentration for 1 h. The plates were washed three times with distilled water and dried under ambient conditions and were used for Raman measurements. This procedure will result the uniform coating of CV molecules over SL films and ensured that excess molecules, if any, were washed away. We could detect CV clearly even at 10^{-8} M. Figure 5 shows the SERS spectrum of CV collected from the surface of Au@MSA SL using 532 nm excitation with an acquisition time of 4 s.

All the peaks have been assigned in Table 1 of the Supporting Information (T1). Here (∥) and (⊥) mean the in-plane and out-of-plane vibrations, respectively. None of the Raman features of MSA are manifested.

We also imaged the crystals using the Raman spectrum. For imaging, first we selected an SL triangle of Au@MSA and focused the laser beam on the surface of the triangle. The white light image of the crystal, selected for Raman imaging, was collected (Figure 6A). The edge length of the SL triangle was around 6 μm. The corresponding Raman image of the triangle was mapped using the same excitation laser. The integration time used for imaging was 0.04 s for a scan width of 12 μm × 12 μm. Figure 6B shows the Raman image. In this image, yellow regions are having maximum Raman intensity and red regions have minimum intensity. One of the interesting observations noted here is the difference in the intensity of Raman signal at the surface and at the edge of the crystal. Theoretical studies of triangular nanoparticles (or nanotriangles) have shown that the Raman enhancement is more at the edges compared to the flat surfaces.[57,58] This is because of the larger electric fields at the edges. In our case, besides this effect, we believe that there could be more hot spots at the edges than on the flat surface. This could be due to the reason that a stacked array of the spherical nanoparticles will be exposed at the edges. Note that more interparticle sites will be exposed at the edges,

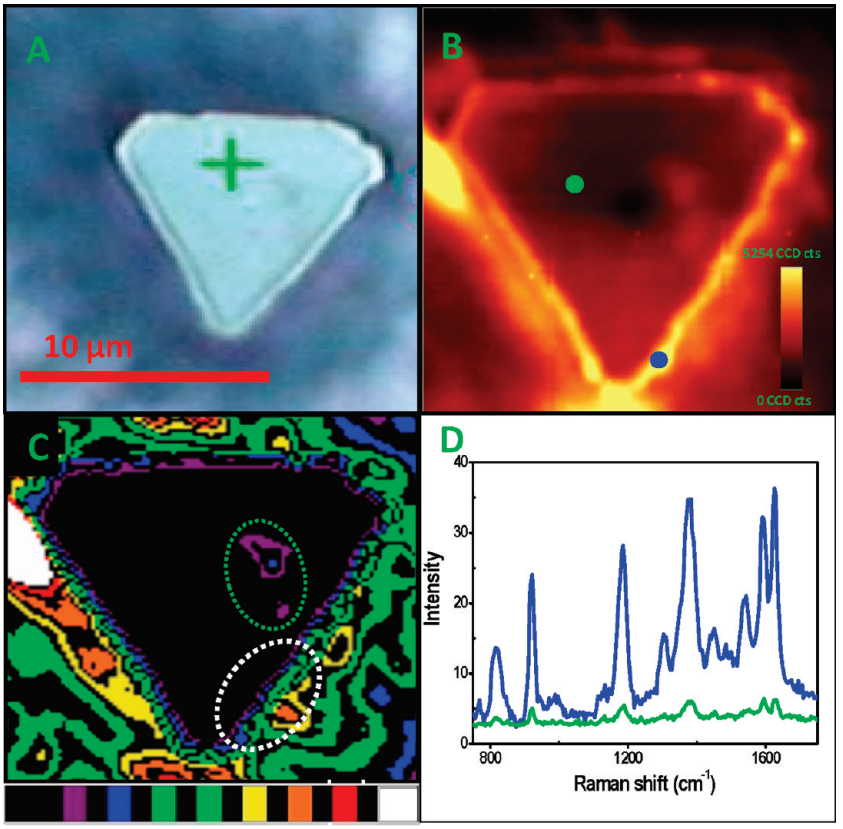

Figure 6. (A) Optical image (under white light illumination) of the Au@MSA SL triangle. (B) Raman image of the same crystal (at 514.5 nm excitation) collected from an area of 12 μm × 12 μm using the intensities of CV features in the 200 to 2000 cm^{-1} window. The concentration of CV exposed was 10^{-5} M. (C) Color coded Raman image of Au@MSA SL triangle shown in part A. The intensity is in the order: green > blue > pink > black. (D) Raman spectra collected from the edge (blue) and surface (green) of the crystal shown in part B.

which will create more hot spots there. In our knowledge, this is the first report showing Raman enhancement in 3D SL crystals. We collected the Raman spectra from the edge and the flat surface of the triangle shown in Figure 6B. Figure 6D shows the corresponding Raman spectra. The intensity of the spectrum collected from the surface is lower than that compared to that collected from the edge, with identical conditions. The Raman spectrum from SL alone, without the adsorbed CV, is very weak and only faint images could be collected using the integrated intensities.

To understand the difference in the enhancement at the edge, we converted the same image into a color coded Raman image. One of the interesting things with color coding is that it can give a different color even for a very small intensity difference. Figure 6C shows the color coded Raman image of same triangle shown in part B. The intensity is in the order: green > blue > pink > black. In this particular crystal, at specific areas of the surface (marked by green circle), we can see larger enhancement. This could be due to the hot spots created by the defects, such as overgrowth or depression. Such defects are seen in SEM images. The color coded Raman image is more informative than the normal Raman image. It may be mentioned that the algorithm faithfully reproduces the features well as long as the spectral intensities are significant as in this case. Such color coded images have to be used with caution so that they are not overinterpreted.

The analyte molecules were adsorbed on SLs by a solution phase deposition method. This ensured uniform adsorption of the molecules. All the Raman measurements were done using the confocal mode. In this, we collect signals from analyte molecules at one plane and all the other layers do not contribute to the data. If there is no field enhancement at the edges, we expect uniform intensity throughout the entire surface of the SL crystals, including edges. Also we observed different intensities from the three different edges of the triangular SL. The Raman intensity collected from the edge "c" is lesser than that from the other two edges: "a" and "b" (see the Supporting Information Figure S5). Theoretical studies suggest that electric field enhancement near the triangular nanoparticles is prominent at the corners and edges.[57,58] Depending on the simulation condition, enhancement could vary at edges and corners.[67] The observed experimental results are in good agreement with the previously reported simulations,[67−70] which confirm the electric field enhancement at edges. These explanations confirm that field enhancement at the edges of the SL triangles is responsible for the larger Raman intensity observed at

(67) Hao, E.; Schatz, G. C. *J. Chem. Phys.* **2004**, *120*, 357.
(68) Kurg, J. T. II; Sanchez, E. J.; Xie, X. S. *J. Chem. Phys.* **2002**, *116*, 10895.
(69) Kottmann, J. P.; Martin, O. J. F.; Smith, D. R.; Schultz, S. *New. J. Phys.* **2000**, *2*(27), 1.
(70) Previte, M. J. R.; Aslan, K.; Gedder, C. D. *Anal. Chem.* **2007**, *79*, 7042.

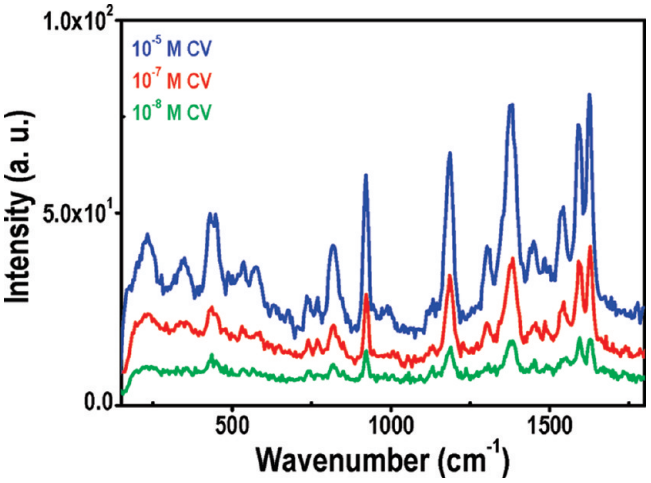

Figure 7. SERS spectra of CV collected from the surface of Au@SGAN SL crystals, excited using 532 nm, with an acquisition time of 4 s. The detection limit of CV was $\sim 10^{-8}$ M.

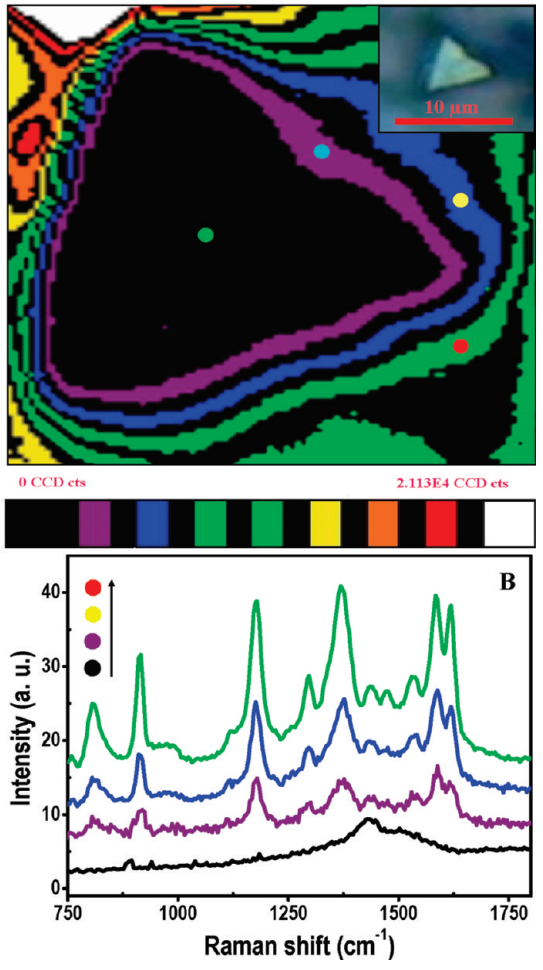

Figure 8. (A) Color coded Raman image (at 514.5 nm excitation) of Au@SGAN SL triangle shown in the inset, acquired using the intensities of the CV in the 200−2000 cm^{-1} window. The CV concentration was 10^{-5} M. The intensity is in the order: green > blue > pink. At the surface, it shows black color having the least intensity. (B) Raman spectra collected from different points shown in part A. Black color is used between two distinctly colored regions at the sides to enhance the image.

the edges and this is not due to higher concentration of the analyte molecules at the edges.

We also studied the SERS of CV by adsorbing it on the surface of Au@SGAN SL triangles. Here also, we could detect CV even at 10^{-8} M. The Raman spectra of CV at different concentrations collected from the surface of Au@SGAN SL are given in Figure 7. The Raman signals are weaker compared to those in Figure 5. No −SGAN feature was detected as in the case of Au@MSA SL.

Using the Raman spectrum, we mapped the corresponding Raman image of Au@SGAN particle crystal. Figure 8A shows the image of a triangle shown in the inset (optical image under white light illumination). We collected the spectrum from different spots shown in Figure 8A. All the spectra collected are shown in Figure 8B. As in the case of Au@MSA, here also we got minimum intensity from the surface and maximum intensity from the edges. Au@SGAN crystals with depression or overgrowth show better enhancement at these locations than the flat surfaces. The images are given in the Supporting Information (Figure S6).

Enhancement Factor (EF) Calculation. In order to calculate the enhancement factor (EF) of these nanoparticle crystals, we compared the measured SERS intensities with those of normal Raman scattering. The EF was calculated as

$$\mathrm{EF} = (I_{\mathrm{SERS}}/I_{\mathrm{norm}})(N_{\mathrm{bulk}}/N_{\mathrm{surf}}) \qquad (1)$$

Where I_{SERS}, I_{norm}, N_{bulk}, and N_{surf} are the measured SERS intensities for a monolayer of probe molecules (CV) on the Au nanoparticle SL surfaces, the measured intensity of nonenhanced or normal Raman scattering from a bulk sample, the number of the probe molecules under laser illumination for the bulk sample, and the number of the probe molecules on SL, respectively. I_{SERS} and I_{norm} are the integral intensities of the *N*-phenyl stretching peak (at 1379 cm^{-1}). N_{bulk} and N_{surf} values were calculated on the basis of the estimated density of the surface species or bulk sample and the corresponding sampling areas. N_{surf} and N_{surf} can be calculated from $N_{\mathrm{surf}} = 4\pi r^2 CAN$ and $N_{\mathrm{surf}} = Ah\rho/M$, where r, C, A, and N are the average radius of the nanoparticles in the SL crystal, surface density of the CV monolayer, the area of the laser spot, and the surface coverage of the Au nanoparticles (particles/μm^2) in the SL crystal, respectively. A, h, ρ, and M are the area of the laser spot, the penetration depth, the density of solid CV (~0.83 g cm^{-3}), and the molecular weight of CV, respectively. For the SL formation, we used 8.5 nm diameter particles, and therefore, the radius is 4.25 nm. The surface coverage of nanoparticles in the SL crystals was measured from the corresponding FESEM images, and it comes around 1000 nanoparticles per squared micrometer. The area of the laser spot used was around 1 μm^2.

The values of EF for Au@MSA and Au@SGAN SLs came around 1.47×10^6 and 3.60×10^5, respectively. The EF of Au@MSA is of the order of 10^6, and it is higher than that of Au@SGAN SLs. This could be due to the small size of the MSA molecule compared to HSGAN. This is reflected in the SL lattice parameters, which were larger for Au@SGAN. This reduces the electromagnetic field experienced by the analyte species for this SL.

Conclusions

We developed a cheap and rapid method for the formation of 3D SLs of Au@SGAN and Au@MSA in gram scale at a liquid−liquid interface under nitrogen gas flow. The morphologies and structures of these crystals were characterized using SEM and HRTEM, respectively. Stacking of nanoparticles in these SLs was measured using SAXS. Interplanar spacing for the (111) and (220) planes of Au@MSA SLs are 10.5 and 6.4 nm, respectively, and for Au@SGAN SLs, the values are 12.5 and 7.5 nm, respectively. The lattice parameters are in good agreement with HRTEM data. These crystals were used as SERS substrates for the detection of crystal violet (CV) with a detection limit of 10^{-8} M. SERS spectra were used to map the corresponding Raman images of these crystals. SERS enhancement was found to be more for the edges of the triangles compared to the flat surfaces which are in agreement with theoretical reports. The enhancement factors were of the order of 1.47×10^6 and 3.60×10^5 for Au@MSA and Au@SGAN SL triangles, respectively. Larger enhancement from the Au@MSA SL trianlges could be explained by considering the small chain length of MSA compared to HSGAN. This will help in the closer approach CV molecules to the hot spots created by the adjacent nanoparticles in the SL triangles. To increase the enhancement factors in SLs, three possible approaches may be used: (1) silver vs gold superlattices, (2) smaller chain length molecules to have greater contact between the particles, and (3) anisotropic particles and their superlattices. All of these approaches are being pursued in the group currently.

Acknowledgment. The authors thank the Department of Science and Technology (DST), Government of India, for constantly supporting our research program on nanomaterials. Mr. Mohammed Akbar Ali, Dept. of Chemistry, IIT Madras, is thanked for calculations using density functional theory (B3LYP/6-31G*). E.S.S. thanks the University Grants Commission (UGC) for a senior research fellowship. Prof. C. N. R. Rao is thanked for permitting the use of his SAXS apparatus. Neenu Varghese and Dr. Kanishka Biswas are thanked for assistance with the SAXS measurements.

Supporting Information Available: Photograph of the setup, HRTEM images of Au@SGAN and Au@MSA nanoparticles, large area SEM image of Au@MSA SL, SEM and EDAX images of the Au@MSA SL triangle, assignment of Raman bands of the SERS spectrum of CV, Raman spectra collected from three different edges of Au@MSA SL triangles with its corresponding 3D Raman image, and color coded Raman images of Au@SGAN SLs showing defects on the flat surface. This material is available free of charge via the Internet at http://pubs.acs.org.